



## Effect of Mo content on microstructure and mechanical properties of CoCrFeNi Series high-entropy alloys

Chunxia Han<sup>a</sup>, Yun Zhang<sup>b, \*\*</sup>, Jingshun Liu<sup>a,\*</sup>, Ze Li<sup>a</sup>, Yanan Wu<sup>a</sup>, Yaqiang Cui<sup>a</sup>, Feng Wang<sup>a</sup>, Zetian Liu<sup>c</sup>

<sup>a</sup> School of Materials Science and Engineering, Inner Mongolia University of Technology, Hohhot, 010051, People's Republic of China

<sup>b</sup> Instrumentation Engineering Faculty, Belarusian National Technical University, Minsk, 220013, Belarus

<sup>c</sup> School of Materials Science and Engineering, Hebei University of Technology, Tianjin, 300401, People's Republic of China



### ARTICLE INFO

#### Keywords:

High-entropy alloys (HEAs)  
Microstructure  
Mechanical properties  
Second phase strengthening  
Nanoindentation hardness

### ABSTRACT

In this paper, the microstructure and mechanical properties of CoCrFeNiMo<sub>x</sub> ( $x = 0, 0.1, 0.3, 0.5, 0.7$ , and  $1.0$ ) high-entropy alloys (HEAs) prepared with high-vacuum arc melting method were studied in detail. After Mo-doping, the strengthening mechanism of HEAs mainly included the component segregation strengthening and the second phase strengthening. Cr and Mo elements were enriched at the grain boundary of HEAs, which led to the formation of  $\sigma$  phase and strengthens the alloys. The microhardness and strength increased with Mo contents, while the elongation decreased gradually. Among which, the higher microhardness, yield strength, and ultimate tensile strength of CoCrFeNiMo<sub>0.3</sub> alloy reach 205.96 HV, 292.22 MPa, and 593.25 MPa, respectively, in compared with other alloys. More importantly, the percentage elongation of which remains 37.36%, and the microhardness distribution was uniform with an average value of 7.4 GPa and an elastic modulus of 263.6 GPa. The research findings presented in this paper could serve as a valuable theoretical basis and practical foundations for the strengthening efforts of face centered cubic (FCC) HEAs.

### 1. Introduction

High-entropy alloys (HEAs) with a stable and simple structure have become the favorable structural materials in recent years due to their advantages of high hardness, high strength, excellent wear resistance and high temperature softening resistance [1–4]. Generally, the increase in the number of alloying elements will inevitably lead to a rise of the mixing entropy in the system, while the high-entropy effect of HEAs will inhibit the appearance of intermetallic compounds, promote the mixing of elements, and finally form simple solid solution structures such as face-centered cubic (FCC), body-centered cubic (BCC) or hexagonal close-packed (HCP) [5–7]. The FCC structure possesses the advantages of large solid solubility and strong adjustability, while the application in engineering structural materials is limited by low strength [8,9].

The incorporation of refractory elements to strengthen HEAs represents a typically promising approach. The addition of elements such as W and Mo to high-entropy alloys can be utilized for solid solution strengthening to increase the strength of the alloys [10,11]. Wu S et al.

found that the element Mo can also slow down the coarsening of the second phase particles [12]. These studies show that the method has wide validity and applicability. CoCrFeNi alloy has become an important research branch in HEAs systems for its excellent ductility and stability [13–15]. However, the strength of CoCrFeNi alloy is low at ambient temperature, which is difficult to meet the needs of high-strength components. Recent studies have shown that the introduction of a second phase strengthening mechanism in CoCrFeNi FCC alloy can effectively improve its strength, such as B2 phase in Al<sub>x</sub>-CoCrFeNi alloys [16,17], L1<sub>2</sub> phase in (CoCrFeNi)<sub>94</sub>Ti<sub>2</sub>Al<sub>4</sub> alloy [18,19], Nb-rich Laves phase in CoCrFeNiNb<sub>x</sub> alloys [20,21], Ni-Si-rich phase in Co<sub>30</sub>Cr<sub>30</sub>(FeNi)<sub>40-x</sub>Si<sub>x</sub> alloys [22,23], and the phase in CoCrFeNiMo<sub>x</sub> alloys [24,25]. However, it is difficult to control the composition of the L1<sub>2</sub> phase, which makes it more prone to the formation of brittle phases during the aging process, resulting in increased alloy brittleness. In addition, the formation of Laves phase and  $\sigma$  phase in the interdendrites reduces the plasticity of HEAs, and it is difficult to control its quantity and distribution during alloy solidification. With the addition of alloying

\* Corresponding author.

\*\* Corresponding author.

E-mail addresses: [zhang\\_yun1991@foxmail.com](mailto:zhang_yun1991@foxmail.com) (Y. Zhang), [jingshun\\_liu@163.com](mailto:jingshun_liu@163.com) (J. Liu).

elements, HEAs are more prone to element segregation during solidification: Heczko and Hasan et al. [26,27] have found that the segregation of Ni and Mn elements in CrMnFeCoNi alloys will affect the structure of the alloy. Liu et al. [28] have found that solute segregation in CrMnFeCoNi alloy would produce a solute drag effect to strengthen the alloy. Accordingly, exploring the co-strengthening effect of the solute segregation prior to precipitation and the second phase particles on the alloy may be an important part of strengthening the FCC HEAs and may further clarify the second phase strengthening mechanism.

In this paper, the characteristics as for Mo element can form hard intermetallic compounds with Cr, Fe, Ni, and Co elements was explored [29]. The effect of Mo content on the microstructure and mechanical properties of as-cast CoCrFeNiMo<sub>x</sub> alloys were investigated systematically. And the alloy with the better matching strength and plasticity were studied. Combined with the composition enrichment and solute segregation after adding Mo element, the strengthening mechanism of the HEAs is illustrated, which could provide a theoretical basis for the second phase strengthening mechanism of HEAs.

## 2. Experimental details

The CoCrFeNiMo<sub>x</sub> ( $x = 0, 0.1, 0.3, 0.5, 0.7$ , and  $1.0$ ) alloys were synthesized by magnetron tungsten electrode high-vacuum arc melting furnace with high-purity Ar as the protective gas. The chemical composition of alloys system is shown in Table 1. For convenience, they were referred to as Mo0, Mo0.1, Mo0.3, Mo0.5, Mo0.7, and Mo1.0 alloy, respectively. The master alloys with a purity of 99.9% was repeatedly smelted 6–8 times by magnetic stirring to ensure homogeneity. The alloy was cast into a plate-like alloy with a size of  $50\text{ mm} \times 40\text{ mm} \times 10\text{ mm}$  by a copper mold. The samples were processed by wire-cut electrical discharge machining (WEDM), as shown in Fig. 1. It has been shown that the phases formed as-cast is quite stable and not far away from the equilibrium state. Therefore, this paper only discussed the microstructure and mechanical properties of as-cast alloys [30–32].

The phase structure of the alloy sample was detected by D/max-2500 X-ray diffractometer (XRD) with radiation source of Cu target  $K\alpha$  ray ( $\lambda = 0.1542\text{ nm}$ ), diffraction angle ( $2\theta$ ) scanning range of  $20^\circ$ – $100^\circ$  and scanning speed of  $4^\circ\text{ min}^{-1}$ . The SETARAM Labsys Evo differential scanning calorimeter was adapted to analyze the phase transition temperature of the alloy sample when it melted or solidified in  $\text{Al}_2\text{O}_3$  crucible, with the main technical parameters as follows: the test temperature range is 298 K–1723 K, the heating and cooling ratio are

both  $10\text{ K min}^{-1}$ , and the mass range of the test samples is 30 mg–50 mg. The sample was polished with 2000-grain SiC sandpaper, followed by mechanical polishing until there were no scratches on the surface, and then corroded with aqua regia for 3 s–10 s. The microstructure of alloys was characterized using a FEI QUANTA 650 FEG scanning electron microscope (SEM) with an energy dispersive spectrometer (EDS).

The microhardness of samples was tested by FM-810 Vickers hardness tester, with a diamond indenter, a loading force of 1000 gf, and a holding time of 15 s. The G200X type nanoindentation instrument was employed to conduct nanoindentation hardness with the indenter of a Berkovich diamond indenter. A  $75 \times 75$  nanoindentation array experiment was carried out. The indentation interval was  $2\text{ }\mu\text{m}$ , the target load was  $7.5\text{ mN}$ , the loading rate was  $0.2\text{ mN s}^{-1}$ , the indentation depth was 200 nm, and the loading time was 10 s. The dog-bone-shaped tensile sample with a cross-section of  $1\text{ mm} \times 1\text{ mm}$  and a length of 16 mm was prepared by WEDM, and the tensile test was carried out by an Instron 5944 electronic universal tensile testing machine with a tensile rate of  $0.42\text{ mm min}^{-1}$  with a maximum equipment sensor loading of 2000 N.

## 3. Results and discussion

### 3.1. XRD analysis

XRD patterns of as-cast CoCrFeNiMo<sub>x</sub> HEAs is shown in Fig. 2. All the alloys display A1-type FCC solid solution matrix because that the high mixing entropy effect of multi-components can effectively reduce the Gibbs free energy of the system and promote the formation of FCC solid solution during solidification. As can be seen from Fig. 2a), the Mo0 and Mo0.1 alloys show only a single FCC phase diffraction peak, and the diffraction peaks of (111) and (200) crystal planes of Mo0.1 alloy decrease obviously. This may be due to the lattice distortion caused by the dissolution of Mo into the matrix [33,34]. The weak diffraction peaks of the  $\sigma$  phase in Mo0.3 and Mo0.5 alloys appear next to the (111) diffraction peak. The structure of  $\sigma$  phase is similar to the tetragonal structure of FeCrMo alloy. According to the electron hole theory of superalloys, the appearance of  $\sigma$  phase can be predicted when the average electron hole number of the alloy is  $> 2.50$  [35]. The average electron hole number of the Mo0.3 alloy was calculated to be 2.57 [36], which indicates that a  $\sigma$  phase may form in Mo0.3 alloy. The  $\sigma$  phase diffraction peaks are enhanced in the Mo0.5 alloy, which indicates that the  $\sigma$  phase content is increased. The weak diffraction peaks of  $\mu$  phase in Mo0.7 and Mo1.0 alloys appear on the left side. The structure of  $\mu$  phase is close to the rhombohedral structure of  $\text{Co}_7\text{Mo}_6$ . When the Mo content exceeds the solubility limit of the matrix, the Mo element precipitated with the form of  $\sigma$  phase intermetallic. As the Mo content continues to increase, the  $\sigma$  phase is partially transformed into the  $\mu$  phase by releasing the lattice strain [24]. The lattice constants of FCC phase in all alloys' matrix increase from  $3.5911\text{ \AA}$  to  $3.6156\text{ \AA}$  because the atomic radius of the Mo ( $1.39\text{ \AA}$ ) element is larger than that of Co ( $1.25\text{ \AA}$ ), Cr ( $1.28\text{ \AA}$ ), Fe ( $1.26\text{ \AA}$ ), and Ni ( $1.24\text{ \AA}$ ) [37]. And the Mo element is dissolved in the FCC matrix so that the FCC diffraction peak in the XRD pattern is obviously shifted to the left to some extent, as shown in Fig. 2b). This observation aligns with the findings of Zin et al. [38], which could be attributed to the lattice distortion caused by the substitution of Co, Cr, Fe, and Ni with the larger Mo atoms [34].

### 3.2. DSC analysis

Fig. 3 shows the DSC heating and cooling curves of as-cast CoCrFeNiMo<sub>x</sub> alloys from 298 K to 1723 K. It can be observed that the melting point of the alloy initially decreases and then increases with an increase of Mo content, which is consistent with the pseudo-binary phase diagram mentioned in Ref. [25]. This is attributed to the large radius of Mo atoms, which causes serious lattice distortion when dissolved into the alloy. This leads to the instability of the crystal structure of the matrix, thereby reducing the melting point of the alloy. However, when the Mo

**Table 1**  
Chemical composition of as-cast CoCrFeNiMo<sub>x</sub> ( $x = 0, 0.1, 0.3, 0.5, 0.7$ , and  $1.0$ ) alloys (at.%).

As-cast Alloys	Phase	Co at. %	Cr at. %	Fe at. %	Ni at. %	Mo at. %
Mo0	Nominal	25	25	25	25	–
	Matrix	25.50	24.62	25.36	24.52	
	GB	23.04	29.08	23.61	24.27	
Mo0.1	Nominal	24.39	24.39	24.39	24.39	2.44
	Matrix	23.63	25.48	23.76	24.18	2.94
	GB	22.10	27.61	22.32	22.58	5.38
Mo0.3	Nominal	23.26	23.26	23.26	23.26	6.96
	Matrix (DR)	23.46	23.42	23.08	22.88	7.16
	IR	18.96	26.50	18.42	16.95	19.18
Mo0.5	Nominal	22.22	22.22	22.22	22.22	11.12
	Matrix (DR)	22.60	21.40	22.96	23.43	9.61
	IR	18.82	24.38	18.39	15.12	23.27
Mo0.7	Nominal	21.28	21.28	21.28	21.28	14.88
	FCC	22.00	20.64	22.31	22.62	12.42
	Eutectic	19.19	22.79	18.66	16.84	22.52
Mo1.0	Nominal	20	20	20	20	
	$\sigma$	17.71	21.25	18.06	14.82	28.16
	Eutectic	18.63	19.62	18.10	17.54	16.10

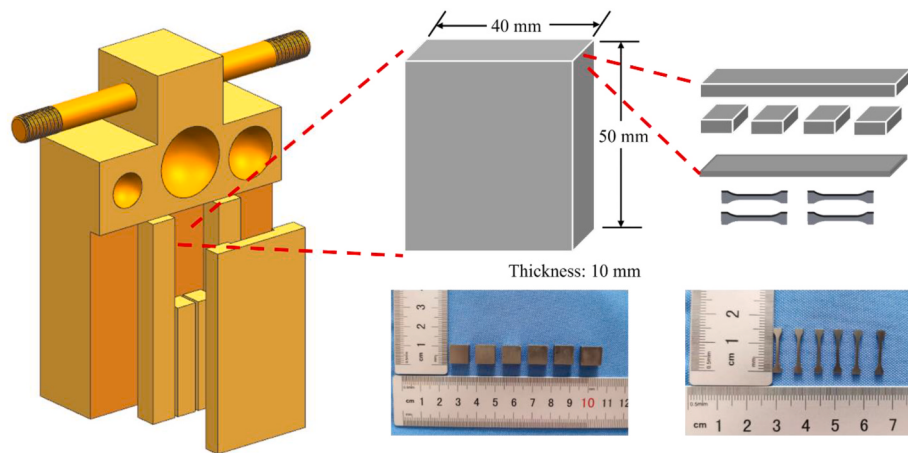


Fig. 1. Schematic diagram and sample size of casting mold of  $\text{CoCrFeNiMo}_x$  HEAs.

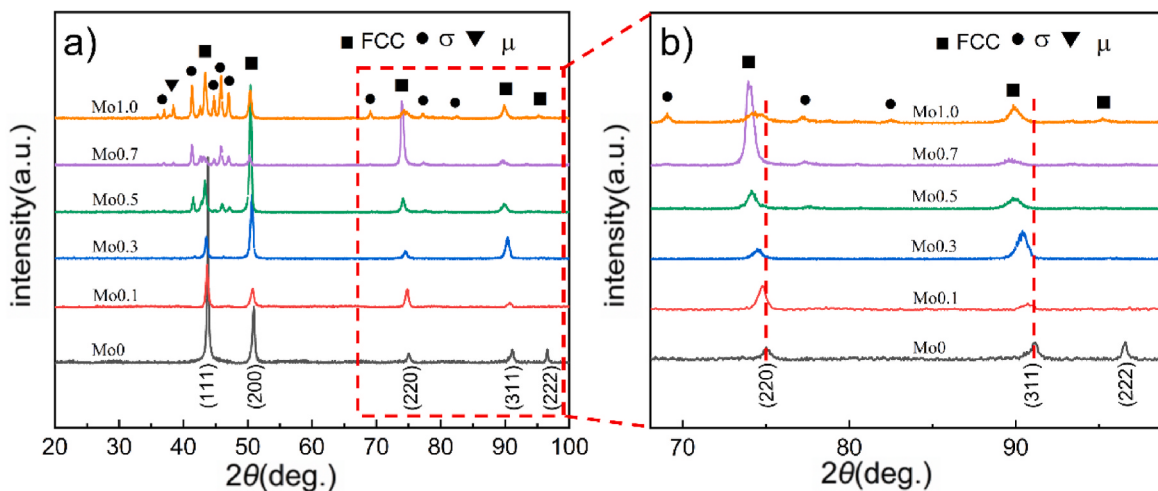


Fig. 2. XRD patterns of as-cast  $\text{CoCrFeNiMo}_x$  HEAs. a) XRD patterns; b) Local magnification.

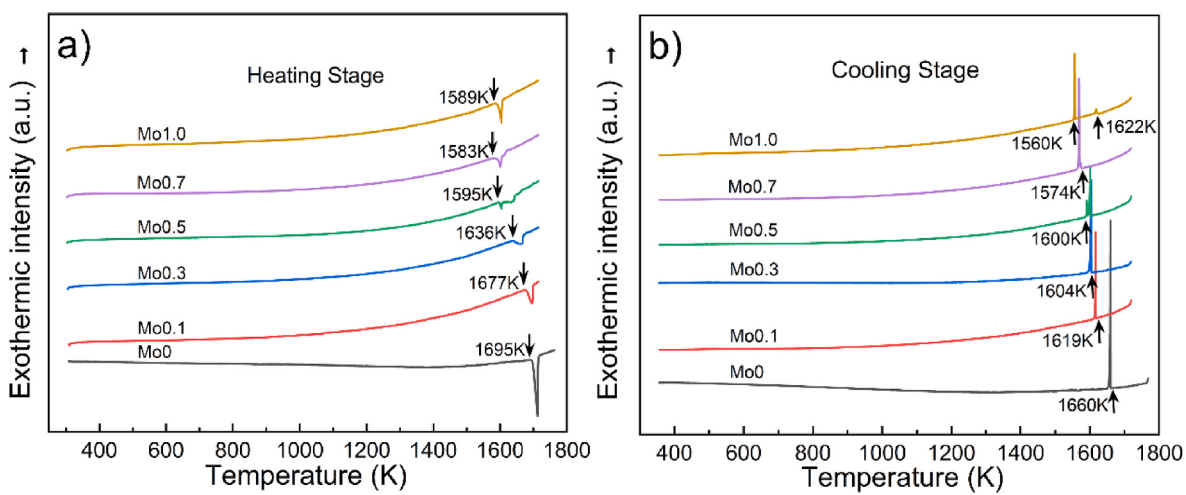


Fig. 3. DSC curves of as-cast  $\text{CoCrFeNiMo}_x$  HEAs. a) Heating stage; b) Cooling stage.

content exceeds the eutectic composition of the alloy, the melting point of the alloy starts to increase. Only one endothermic peak (as seen in Fig. 3a) and one exothermic peak (as seen in Fig. 3b) in both Mo0 and Mo0.1 alloys appear. This indicates that new phase is not formed, which

is consistent with the XRD results. It can be seen from Fig. 3 that the endothermic peak of Mo0.3 alloy is obviously broadened, which is caused by the widening temperature range of alloy melting due to the increase of Mo content. The two adjacent endothermic peaks of Mo0.5

alloy appear. The first peak represents the melting of the interdendritic structure, and the second peak represents the melting of the dendrite structure according to the (CoCrFeNi)-Mo pseudo-binary phase diagram [25]. The two endothermic peaks are close to each other because the composition of dendrite structure is close to the composition of interdendritic structure, which is consistent with the two exothermic peaks, as shown in Fig. 3b). The composition of Mo0.7 alloy is close to the eutectic composition of the pseudo-binary alloy, so the endothermic peak and exothermic peak are the melting peak and solidification peak of the eutectic structure. The structure of Mo1.0 alloy is a hypereutectic structure. The first peak represents the exothermic peak of the primary pro-eutectic  $\sigma$  phase, and the second peak represents the exothermic peak of the eutectic structure according to Cr-Mo-Ni and Cr-Fe-Mo ternary alloy phase diagrams [39].

### 3.3. Microstructure characterization

Fig. 4 presents the optical metallographic structure and SEM morphology of the as-cast CoCrFeNiMo<sub>x</sub> HEAs. It can be seen from Fig. 4 a) and b) that Mo0 alloy exhibits an equiaxed crystal structure, and its chemical composition is close to the nominal composition (Table 1), and the content of Cr element at the grain boundary (GB) is slightly higher. The formation of equiaxed crystal structure is attributed to two reasons. Firstly, Co, Cr, Fe, and Ni elements share similar properties and atomic sizes, which prevent significant component segregation during the solidification process [27]. Secondly, the mixing enthalpy of the six atoms approaches zero [40]. From Fig. 4c) and d), Mo0.1 alloy exhibits a uniform equiaxed dendrite structure. It can be seen from Table 1 that Cr and Mo content at GB are relatively high, which shows that the diffusion of Cr and Mo elements is slow. They are gradually repelled and enriched to the GB during the solidification process. It can be seen from Fig. 4e) and f) that Mo0.3 alloy exhibits a dendrite structure. The EDS energy spectrum and the chemical composition of IR and DR are shown in Fig. 5. The Cr and Mo elements are significantly enriched in the IR than in the DR. Combined with XRD results, both IR and DR were FCC phase, and the  $\sigma$  phase was too small to be found in the interdendritics. It shows that the addition of Mo element leads to composition segregation and

promotes the formation of dendrite structure during the crystallization process of the alloy. This is consistent with the results of Jiang et al. [41, 42]. The dendritic region is formed first in the alloy, and the Cr and Mo elements with slow diffusion are gradually repelled and enriched to form the IR region. It can be seen from Fig. 4g and h) that Mo0.5 alloy exhibits an obvious dendrite structure, and the  $\sigma$  phase with discontinuous network distribution is formed in the IR. From Fig. 4i) and j), the microstructure of Mo0.7 alloy is the hypoeutectic structure of FCC + (FCC +  $\sigma$ ) phase, and the bright white in Fig. 4i) is the pro-eutectic FCC phase. The FCC solid solution crystallizes first, then the remaining liquid phase crystallizes as a lamellar FCC +  $\sigma$  eutectic structure during the solidification process. From Fig. 4k) and l), the microstructure of Mo1.0 alloy is a hypereutectic structure composed of  $\sigma$ +( $\sigma$ +FCC) phase, and the gray-white structure in Fig. 4l) is the pro-eutectic  $\sigma$  phase and the bright part of its edge is the  $\mu$  phase [24]. The  $\mu$  phase appears at the edge of  $\sigma$  phase, indicating that it is formed by the transformation of the  $\sigma$  phase during solidification. The  $\sigma$  phase crystallizes first, then the remaining liquid phase crystallizes as a lamellar  $\sigma$  + FCC eutectic structure during the solidification process of the alloy. Excessive Mo element increases the amount of the  $\sigma$  phase and the lattice strain. While the Mo content is 1.0, the huge lattice stress makes the  $\sigma$  phase unable to maintain its tetragonal structure, and the release of lattice strain results in the transformation of a portion of the  $\sigma$  phase into the rhombohedral structure  $\mu$  phase.

In practice, the solidification process of CoCrFeNiMo<sub>x</sub> HEAs gradually deviates from the equilibrium condition due to the fast-cooling rate and the diffusion rates of each component in the alloy. The alloy gradually forms a dendritic structure and leads to different chemical compositions between the pre-crystallized dendrites and the post-crystallized interdendritics. Therefore,  $\sigma$  phase is formed when the amount of Cr and Mo elements in the interdendritics is sufficient.

### 3.4. Mechanical properties

Both the microhardness of CoCrFeNiMo<sub>x</sub> HEAs and nanoindentation test results of Mo0.3 alloy is exhibited in Fig. 6. It can be seen from Fig. 6a) that the microhardness of the alloy gradually increases with

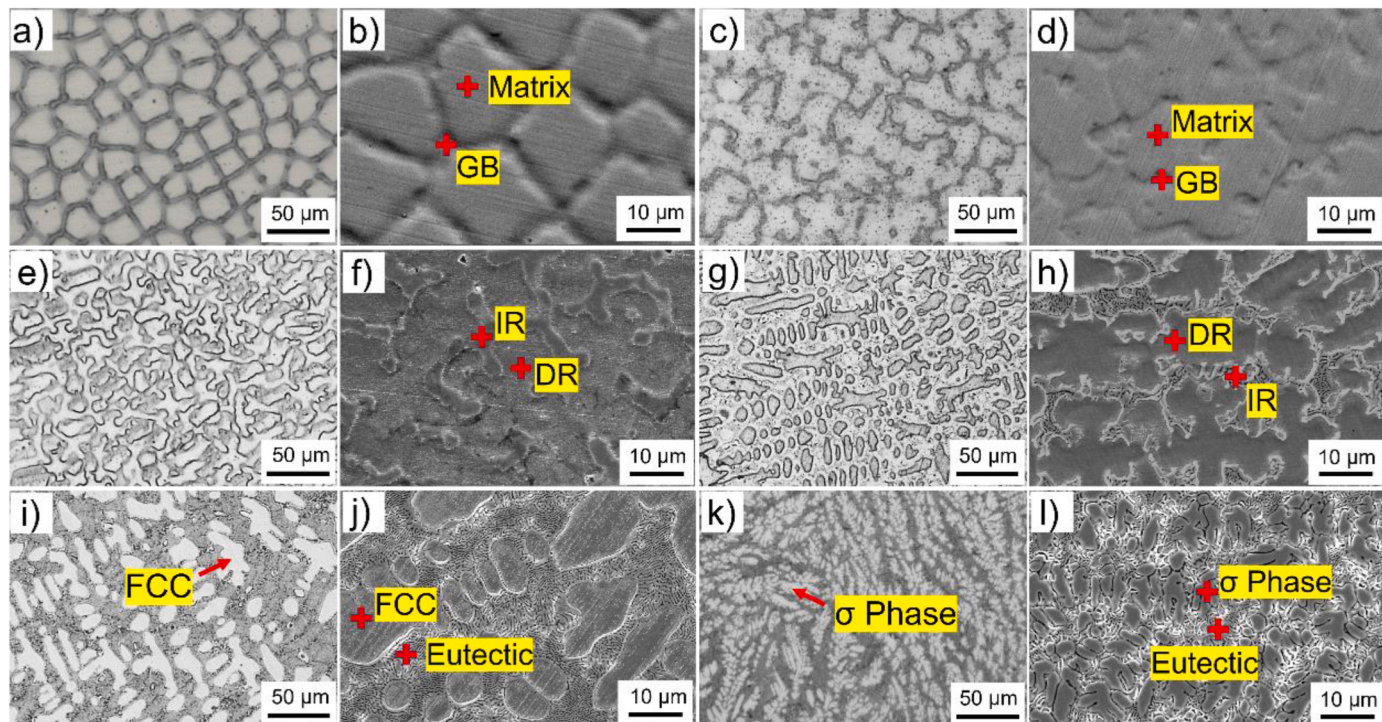


Fig. 4. Optical microscopy image and SEM morphology of as-cast CoCrFeNiMo<sub>x</sub> HEAs. a), b) Mo0; c), d) Mo0.1; e), f) Mo0.3; g), h) Mo0.5; i), j) Mo0.7; k), l) Mo1.0.

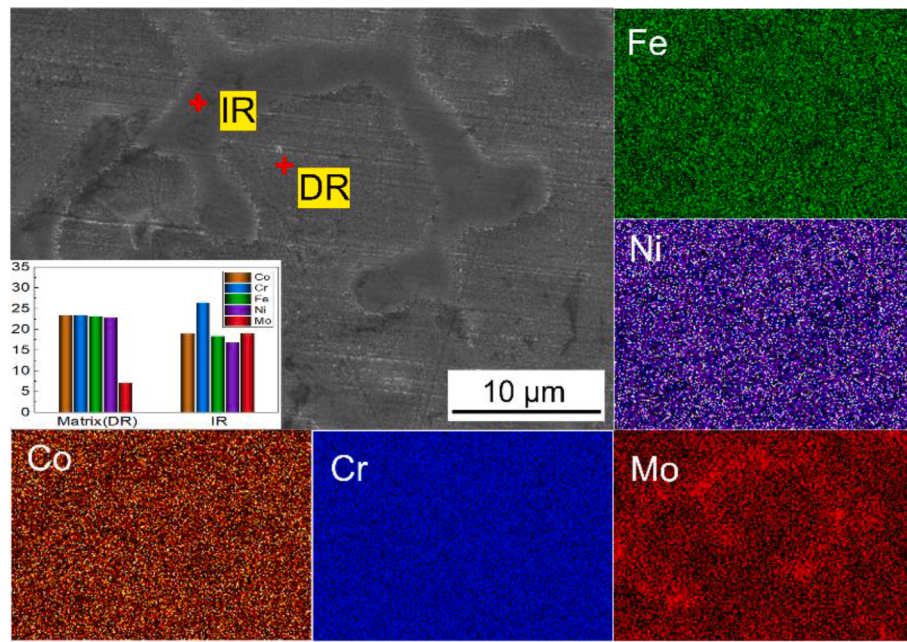


Fig. 5. SEM morphology and EDS spectrum of CoCrFeNiMo<sub>0.3</sub> alloy.

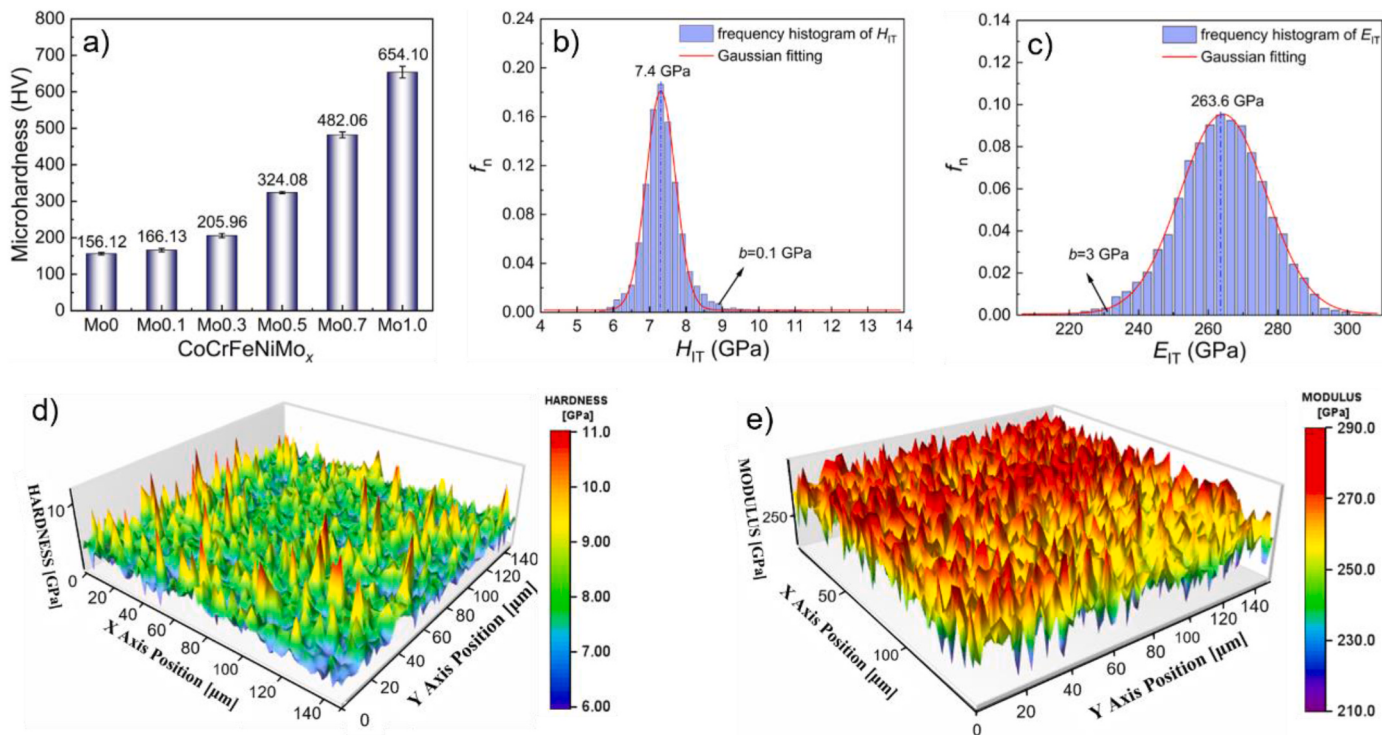


Fig. 6. Microhardness histogram of CoCrFeNiMo<sub>x</sub> HEAs and nanoindentation distribution results of CoCrFeNiMo<sub>0.3</sub> alloy. a) Microhardness of HEAs; b) Gaussian distribution fitting results of  $H_{IT}$  histograms; c) Gaussian distribution fitting results of  $E_{IT}$  histograms; d) 3D mapping of hardness; e) 3D distribution of elastic modulus.

increasing of Mo content. The microhardness of alloys rises due to the solid solution strengthening of Mo element and its segregation at the grain boundaries with the increase of Mo addition from 0 to 0.3. The microhardness continues to increase due to the formation of more  $\sigma$  phases as the Mo content increases from 0.5 to 1.0. The microhardness of  $\sigma$  phase at room temperature is higher than HV1100 [43]. It is noteworthy that the hardness value of the Mo<sub>0.3</sub> alloy reaches 205.96 HV, which is an increase of 23.98% over the Mo<sub>0.1</sub> alloy.

Fig. 6b)-e) show the results of nanoindentation hardness test on the Mo<sub>0.3</sub> alloy. The Gaussian model fitting result of the frequency histogram is a probability density curve, and the ordinate is the normalized probability density  $f_n$  represented by the relative frequency divided by the group distance  $b$  (bin size, marked in Fig. 6b). According to Fig. 6b) and c), they exhibit a unimodal distribution and are consistent with the 3D distribution shown in Fig. 6d) and e). The average nanoindentation hardness and elastic modulus are 7.4 GPa and 263.6 GPa, respectively.

Since the nanoindentation hardness value of alloy is lower than 9.4 GPa of the  $\sigma$  phase in Ref. [44], it is hypothesized that a small amount of the nano- $\sigma$  phase is generated in Mo0.3 alloy.

Fig. 7 represents the tensile stress-strain curves and mechanical properties for the CoCrFeNiMo<sub>x</sub> HEAs. As the Mo content increases from 0 to 0.7, the yield strength and tensile strength of the alloy increase from 201.74 MPa to 441.65 MPa–855.88 MPa and 1050.89 MPa, respectively. However, the Mo1.0 alloy decreases to 562.56 MPa and 619.71 MPa, respectively. And the elongation decreases from 69.18% to 2.45%. According to both the XRD patterns and SEM images, the  $\sigma$  and  $\mu$  phases have a lattice misfit with the FCC matrix because of their topologically close-packed, which leads to a large accumulation of dislocations at the interface and induces stress concentration and cracking during the tensile process. Therefore, the tensile strength increases while the elongation decreases. The strength of Mo1.0 alloy decreases especially because of the phenomenon of low stress brittle fracture. Excessive brittle phases are formed in the alloy. The stress is concentrated at the interface between the second phase and the matrix, leading to the rapid generation and extension of cracks, resulting in the fracture of the alloy during the tensile process. The strengthening of the CoCrFeNiMo<sub>x</sub> HEAs is attributed to both the solid solution strengthening and the formation of  $\sigma/\sigma + \mu$  phases. Among them, Mo0.3 alloy shows moderate tensile strength and elongation.

Fig. 8 exhibits the tensile fracture SEM morphology of as-cast CoCrFeNiMo<sub>x</sub> HEAs. From Fig. 8a), it is evident that the Mo0 alloy undergoes significant necking during deformation. Additionally, the fracture surface is characterized by a multitude of densely distributed dimples. From Fig. 8b), the fracture dimples of the Mo0.1 alloy are large and deep, and the distribution is uniform. This indicates that the Mo0 and Mo0.1 alloys both have excellent plasticity, are typical plastic fractures. The fracture dimples of Mo0.3 alloy are irregular, small, and shallow, indicating that its plasticity is relatively lower than that of Mo0.1 alloy, as shown in Fig. 8c). The fracture morphology of Mo0.5 alloy exhibits significant undulations and contains small cleavage planes, showing a rock-like fracture pattern as shown in Fig. 8d). This is due to the formation of  $\sigma$  phase in the interdendrites, which alters the path of crack extension. Both Mo0.7 and Mo1.0 alloys exhibit obvious cleavage planes, indicating that they both have poor plasticity as shown in Fig. 8e) and f). The excess  $\sigma$  phase in alloys disrupts the continuity of the matrix, becoming a source of cracks during tensile process, ultimately impairing the plasticity of the alloy. The fracture of Mo1.0 alloy clearly displays river-like patterns, which are characteristic of typical cleavage fracture.

### 3.5. Strengthening mechanism of HEAs

The Mo0 alloy shows a single FCC structure and an equiaxial crystalline structure, with a yield strength of 201.74 MPa. This is due to that the elements of Co, Cr, Fe, and Ni are similar in nature, and the alloy does not show any obvious compositional segregation during the solidification process. This is consistent with the results of Wang et al. [27, 45]. Dendritic structure appears in the alloy after the addition of Mo elements, and the slower diffusing Cr and Mo elements are gradually excluded from the inter-dendritic region and continuously enriched as shown in Fig. 9a). The yield strength of Mo0.1 alloy is 218.51 MPa, which is slightly higher than that of Mo0 alloy. This is due to the solid solution of Mo elements in the matrix to produce lattice distortion of the alloy, playing the role of solid solution strengthening, which is consistent with Ref. [46]. This is also consistent with the results that the diffraction peaks of (220) and (311) grain surfaces are slightly left shifted in XRD patterns in this paper. The yield strength of Mo0.3 alloy is 292.22 MPa, which is 44.85% higher than that of Mo0.1 alloy. In this paper, it is speculated that a small amount of nano  $\sigma$  phase was generated in the alloy, and a trace amount of  $\sigma$  phase also appeared in the Mo0.3 alloy in Ref. [47]. At this time, more Mo elements were dissolved in the FCC matrix, and the lattice distortion of the alloy increased, and the diffraction peaks of the (220) and (311) crystal planes in XRD patterns were obviously shifted to the left. The alloy strengthening is a synergistic effect of solid solution strengthening and second phase strengthening mechanisms. The yield strength value of Mo0.5 alloy reaches 483.03 MPa, which is 139.43% higher than that of Mo0 alloy, but its plasticity decreases to 9.27%. The increase of  $\sigma$  phase diffraction peaks in the XRD pattern indicates the increase in the amount of the second phase precipitation, which is consistent with the results of the microstructure diagram. The strengthening of the alloy is due to the increase in the amount of the second phase, which also leads to a decrease in the volume fraction of the FCC phase in the matrix, so the plasticity decreases. The yield strength of Mo0.7 alloy reaches 855.88 MPa, and in XRD patterns, the  $\sigma$  phase diffraction peaks are enhanced, and weak diffraction peaks of  $\mu$  phase appear on the left side. The main reason for the strengthening of the alloy is the increased precipitation of the second phase and the generation of the harder  $\mu$  phase [24, 48, 49]. The plasticity of the alloy is further reduced to 5.58% as the second phase is hard and brittle. The yield strength of Mo1.0 alloy decreased to 562.56 MPa and plasticity was 2.45%. The diffraction peaks of  $\sigma$  and  $\mu$  phase of the alloy are enhanced in the XRD pattern, which indicated that the content of  $\sigma$  phase and  $\mu$ -phase were both increased. Combined with the SEM topography, the Mo1.0 alloy is a per-eutectic organization, and its pre-eutectic phase is the  $\sigma$  phase, and the eutectic composition is the

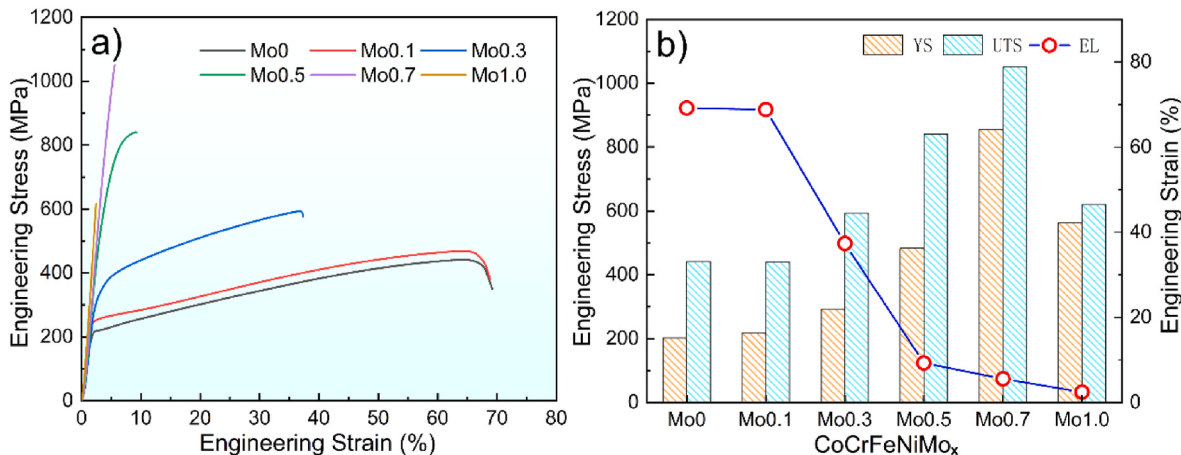
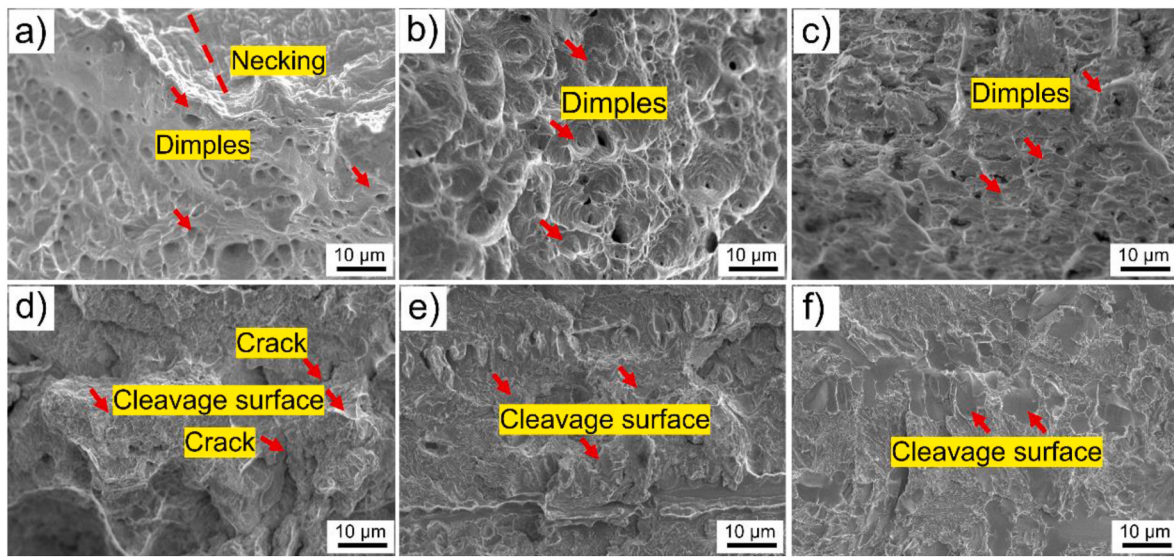
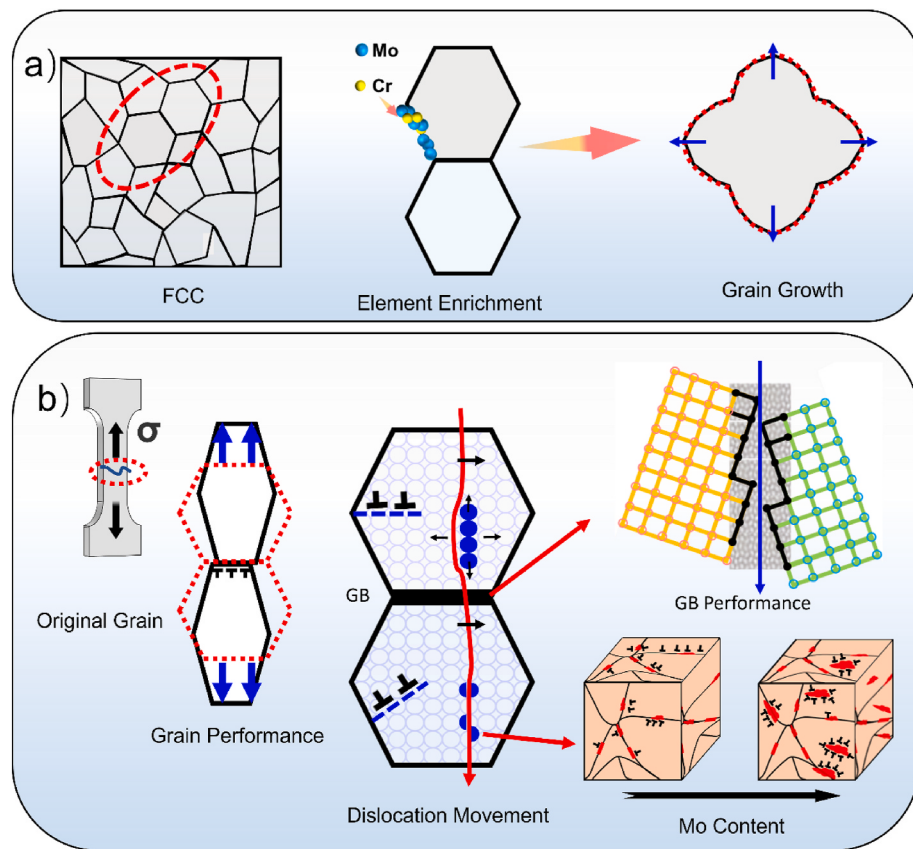


Fig. 7. Stress-strain curves and statistics of mechanical properties of as-cast CoCrFeNiMo<sub>x</sub> HEAs. a) Engineering stress-strain curve; b) Statistical results of YS, UTS and EL.



**Fig. 8.** SEM morphology of tensile fracture of as-cast CoCrFeNiMo<sub>x</sub> HEAs. a) Mo0; b) Mo0.1; c) Mo0.3; d) Mo0.5; e) Mo0.7; f) Mo1.0.



**Fig. 9.** Strengthening mechanism of CoCrFeNiMo<sub>x</sub> HEAs. a) Element enrichment and solid solution strengthening; b) second phase strengthening.

lamellar  $\sigma$  + FCC phase. Therefore, the volume fraction of FCC phase is less than that of Mo0.7 alloy, and the plasticity of the alloy is lower. Since the  $\sigma$  phase is a multi-element solid solution phase and the presence of excess Mo in the Mo1.0 alloy results in a gradual increase in the amount of the  $\sigma$  phase and a gradual increase in the lattice strain. When the  $\sigma$  phase is unable to maintain its tetragonal structure, the release of lattice strain leads to the transformation of part of the  $\sigma$  phase into the rhombic  $\mu$  phase [24,49]. Due to the high content of brittle hard phases in the alloy, cracking during tensile deformation occurs firstly in the

interface between the  $\sigma/\mu$  phase and FCC. Due to the low amount of FCC phase, the cracks expand rapidly as shown in Fig. 9b), leading to the cleavage fracture of the alloy, with a decrease in both strength and plasticity. This is consistent with that shown in Fig. 8f). In summary, the Mo element in CoCrFeNiMo<sub>x</sub> alloy promotes the generation of  $\sigma$  phase, and with the increase of Mo content, the strengthening of the alloy is dominated by solid solution strengthening, which is gradually transformed into solid solution strengthening and the second-phase precipitation strengthening together, and finally dominated by the

second-phase precipitation strengthening.

#### 4. Conclusions

In summarizing, the effect of Mo content on microstructure and mechanical properties of CoCrFeNiMo<sub>x</sub> HEAs is systematically investigated. The following conclusions are drawn.

- (1) With the increase of Mo content, the phase structure evolution of CoCrFeNiMo<sub>x</sub> HEAs change from FCC to FCC+ $\sigma$  and then to FCC+ $\sigma$ + $\mu$ . The strengthening of CoCrFeNiMo<sub>x</sub> HEAs is due to the solid solution of Mo element, the segregation of Cr and Mo elements and the formation of second phase.
- (2) With the increase of Mo content, the hardness and strength of the CoCrFeNiMo<sub>x</sub> HEAs gradually increase while the ductility decrease. Among them, the Mo0.3 alloy exhibits the better match of mechanical properties. In compared with Mo0 alloy, Mo0.3 alloy demonstrates an improvement of 31.41% and 34.33% in hardness and tensile strength, respectively, while the ductility decreases by 46%.
- (3) The Gaussian fitting curves of the frequency histogram of the nanoindentation hardness and elastic modulus of CoCrFeNiMo<sub>0.3</sub> alloy are unimodal. And the average nanoindentation hardness and elastic modulus are 7.4 GPa and 263.6 GPa, respectively.

#### Conflicts of the interest

The authors declare no conflict of interest that could have appeared to influence the work reported in this paper.

#### Declaration of competing interest

The authors declare that they have no known competing financial interests or personal relationships that could have appeared to influence the work reported in this paper.

#### Acknowledgments

This work was financially supported by the National Natural Science Foundation of China (NSFC) under grant nos. 52061035, Young Leading Talent of "Grassland Talents" Project of Inner Mongolia Autonomous Region (no. QNLJ012010), Program for Innovative Research Team in Universities of Inner Mongolia Autonomous Region (no. NMGIRT2211), Inner Mongolia University of Technology Key Discipline Team Project of Materials Science (no. ZD202012).

#### References

- [1] Yeh JW, Chen SK, Lin SJ, Gan JY, Chin TS, Shun TT, et al. Nanostructured high-entropy alloys with multiple principal elements novel alloy design concepts and outcomes. *Adv Eng Mater* 2004;6:299–303. <https://doi.org/10.1002/adem.200300567>.
- [2] Cantor B, Chang ITH, Knight P, Vincent AJB. Microstructural development in equiatomic multicomponent alloys. *Mater Sci Eng* 2004;375:213–8. <https://doi.org/10.1016/j.msea.2003.10.257>.
- [3] Miracle DB, Senkov ON. A critical review of high entropy alloys and related concepts. *Acta Mater* 2017;122:448–511. <https://doi.org/10.1016/j.actamat.2016.08.081>.
- [4] Senkov ON, Miller JD, Miracle DB, Woodward C. Accelerated exploration of multi-principal element alloys with solid solution phases. *Nat Commun* 2015;6:6529. <https://doi.org/10.1038/ncomms7529>.
- [5] Otto F, Dlouhy A, Pradeep KG, Kubenová M, Raabe D, Eggeler G, et al. Decomposition of the single-phase high-entropy alloy CrMnFeCoNi after prolonged anneals at intermediate temperatures. *Acta Mater* 2016;112:40–52. <https://doi.org/10.1016/j.actamat.2016.04.005>.
- [6] Couzinié JP, Dírras G. Body-centered cubic high-entropy alloys from processing to underlying deformation mechanisms. *Mater Char* 2019;147:533–44. <https://doi.org/10.1016/j.matchar.2018.07.015>.
- [7] Zhao YJ, Qiao JW, Ma SG, Gao MC, Yang HJ, Chen MW, et al. A hexagonal close-packed high-entropy alloy: the effect of entropy entropy. *J. Materials and Design* 2016;96:10–5. <https://doi.org/10.1016/j.matdes.2016.01.149>.
- [8] Gludovatz B, Hohenwarter A, Cattoor D, Chang EH, George EP, Ritchie RO. A fracture-resistant high-entropy alloy for cryogenic applications. *Science* 2014;345:1153–8. <https://doi.org/10.1126/science.1254581>.
- [9] Sun SJ, Tian YZ, An XH, Lin HR, Wang JW, Zhang ZF. Ultrahigh cryogenic strength and exceptional ductility in ultrafine-grained CoCrFeMnNi high-entropy alloy with fully recrystallized structure. *Materials Today Nano* 2018;4:46–53. <https://doi.org/10.1016/j.mtnano.2018.12.002>.
- [10] Wu SW, Yang T, Cao BX, Luan JH, Jia YF, Xu L, et al. Multicomponent Ni-rich high-entropy alloy toughened with irregular-shaped precipitates and serrated grain boundaries. *Scripta Mater* 2021;204:114066. <https://doi.org/10.1016/j.scriptamat.2021.114066>.
- [11] Jia YF, Wang G, Wu SW, Mu YK, Yi Y, Jia YD, et al. A lightweight refractory complex concentrated alloy with high strength and uniform ductility. *Appl Mater Today* 2022;27:101429. <https://doi.org/10.1016/j.apmt.2022.101429>.
- [12] Wu SW, Chia HY, Zhang TL, Jia YF, Mu YK, Zhang Q, et al. A precipitation strengthened high entropy alloy with high (Al+ Ti) content for laser powder bed fusion synergizing its intrinsic hot cracking resistance and ultrahigh strength. *Acta Mater* 2023;258:119193. <https://doi.org/10.1016/j.actamat.2023.119193>.
- [13] Lu YP, Dong Y, Jiang H, Wang ZJ, Cao ZQ, Guo S, et al. Promising properties and future trend of eutectic high entropy alloys. *Scripta Mater* 2020;187:202–9. <https://doi.org/10.1016/j.scriptamat.2020.06.022>.
- [14] Man JL, Wu BL, Duan GS, Zhang L, Wan G, Zhang L, et al. The synergistic addition of Al, Ti, Mo and W to strengthen the equimolar CoCrFeNi high-entropy alloy via thermal-mechanical processing. *J Alloys Compd* 2022;902:163774. <https://doi.org/10.1016/j.jallcom.2022.163774>.
- [15] Fan AC, Li JH, Tsai MH. On the phase constituents of three CoCrFeNi<sub>x</sub> (x = Cr, Mo, W) high-entropy alloys after prolonged annealing. *Mater Chem Phys* 2022;276:125431. <https://doi.org/10.1016/j.matchemphys.2021.125431>.
- [16] Wang WR, Wang WL, Wang SC, Tsai YC, Lai CH, Yeh JW. Effects of Al addition on the microstructure and mechanical property of Al<sub>x</sub>CoCrFeNi high-entropy alloys. *Intermetallics* 2012;26:44–51. <https://doi.org/10.1016/j.intermet.2012.03.005>.
- [17] Tokarewicz M, Grasdka-Dahlke M, Recko K, Lipicka M. The influence of annealing at 500 °C and 900 °C on the structure and mechanical properties of Al<sub>x</sub>CoCrFeNi alloys. *Materials* 2023;16:1245. <https://doi.org/10.3390/ma16031245>.
- [18] He JY, Wang H, Wu Y, Liu XJ, Mao HH, Nieh TG, et al. Precipitation behavior and its effects on tensile properties of FeCoNiCr high-entropy alloys. *Intermetallics* 2016;79:41–52. <https://doi.org/10.1016/j.intermet.2016.09.005>.
- [19] Yang T, Zhao YL, Tong Y, Jian ZB, Wei J, Cai JX, et al. Multicomponent intermetallic nanoparticles and superb mechanical behaviors of complex alloys. *Science* 2018;362:933–7. <https://doi.org/10.1126/science.aas8815>.
- [20] Liu WH, He JY, Huang HL, Wang H, Lu ZP, Liu CT. Effects of Nb additions on the microstructure and mechanical property of CoCrFeNi high-entropy alloys. *Intermetallics* 2015;60:1–8. <https://doi.org/10.1016/j.intermet.2015.01.004>.
- [21] Jiang H, Jiang L, Qiao DX, Lu YP, Wang TM, Cao ZQ, et al. Effect of niobium on microstructure and properties of the CoCrFeNb<sub>x</sub> Ni high entropy alloys. *J Mater Sci Technol* 2017;33:712–7. <https://doi.org/10.1016/j.jmst.2016.09.016>.
- [22] Gao XF, Chen Y, Chen RR, Liu T, Fang HZ, Qin G, et al. Tailoring formation and proportion of strengthening phase in non-equiatomic CoCrFeNi high entropy alloy by alloying Si element. *Intermetallics* 2022;147:107617. <https://doi.org/10.1016/j.intermet.2022.107617>.
- [23] Wei DX, Gong W, Tsuru T, Lobzenko I, Li XQ, Harjo S, et al. Si-addition contributes to overcoming the strength-ductility trade-off in high-entropy alloys. *Int J Plast* 2022;159:103443. <https://doi.org/10.1016/j.iplas.2022.103443>.
- [24] Shun TT, Chang LY, Shiu MH. Microstructure and mechanical properties of multiprincipal component CoCrFeNi<sub>x</sub> alloys. *Mater Char* 2012;70:63–7. <https://doi.org/10.1016/j.matchar.2012.05.005>.
- [25] Liu WH, Lu ZP, He JY, Luan JH, Wang ZJ, Liu B, et al. Ductile CoCrFeNi<sub>x</sub> high entropy alloys strengthened by hard intermetallic phases. *Acta Mater* 2016;116:332–42. <https://doi.org/10.1016/j.actamat.2016.06.063>.
- [26] Heczko M, Mazánová V, Gröger R, Záležák T, Hooshmand MS, George EP, et al. Elemental segregation to lattice defects in the CrMnFeCoNi high-entropy alloy during high temperature exposures. *Acta Mater* 2021;208:116789. <https://doi.org/10.1016/j.actamat.2021.116719>.
- [27] Hasan MN, Gu J, Jiang S, Wang HJ, Cabral M, Ni S, et al. Effects of elemental segregation on microstructural evolution and local mechanical properties in a dynamically deformed CrMnFeCoNi high entropy alloy. *Scripta Mater* 2021;190:80–5. <https://doi.org/10.1016/j.scriptamat.2020.08.048>.
- [28] Liu G, Lu DH, Liu XW, Liu FC, Yang Q, Du H, et al. Solute segregation effect on grain boundary migration and Hall-Petch relationship in CrMnFeCoNi high-entropy alloy. *Mater Sci Technol* 2019;35:500–8. <https://doi.org/10.1080/02670836.2019.1570679>.
- [29] Lyu ZY, Lee C, Wang SY, Fan XS, Yeh JW, Liaw PK. Effects of constituent elements and fabrication methods on mechanical behavior of high-entropy alloys: a review. *Mettal Mater Trans* 2019;50A:1–28. <https://doi.org/10.1007/s11661-018-4970-z>.
- [30] Wen LH, Kou HC, Li JS, Chang H, Xue XY, Zhou I. Effect of aging temperature on microstructure and properties of AlCoCrCuFeNi high-entropy alloy. *Intermetallics* 2009;17:266–9. <https://doi.org/10.1016/j.intermet.2008.08.012>.
- [31] Senkov ON, Wilks GB, Scott JM, Miracle DB. Mechanical properties of Nb<sub>25</sub>Mo<sub>25</sub>Ta<sub>25</sub>W<sub>25</sub> and V<sub>20</sub>Nb<sub>20</sub>Mo<sub>20</sub>Ta<sub>20</sub>W<sub>20</sub> refractory high entropy alloys. *Intermetallics* 2011;19:698–706. <https://doi.org/10.1016/j.intermet.2011.01.004>.
- [32] Lin CM, Tsai HL. Equilibrium phase of high-entropy FeCoNiCrCu<sub>0.5</sub> alloy at elevated temperature. *J Alloys Compd* 2010;489:30–5. <https://doi.org/10.1016/j.jallcom.2009.09.041>.
- [33] Yeh JW, Chang SY, Hong YD, Chen SK, Lin SJ. Anomalous decrease in X-ray diffraction intensities of Cu-Ni-Al-Co-Cr-Fe-Si alloy systems with multi-principal

- elements. *Mater Chem Phys* 2007;103:41–6. <https://doi.org/10.1016/j.matchemphys.2007.01.003>.
- [34] Miao JW, Guo TM, Ren JF, Zhang AJ, Su B, Meng JH. Optimization of mechanical and tribological properties of FCC CrCoNi multi-principal element alloy with Mo addition. *Vacuum* 2018;149:324–30. <https://doi.org/10.1016/j.vacuum.2018.01.012>.
- [35] Shun TT, Chang LY, Shiu MH. Microstructures and mechanical properties of multiprincipal component CoCrFeNiTi<sub>x</sub> alloys. *Mater Sci Eng, A* 2012;556:170–4. <https://doi.org/10.1016/j.msea.2012.06.075>.
- [36] Li MY, Guo LH, Li JL, Zhang Q, Han B, Song LX. Effect of ultrasonic impact treatment on the microstructure and properties of laser cladded CoCrFeNiMo<sub>x</sub> high entropy alloy coatings. *Surf Coating Technol* 2024;476:130243. <https://doi.org/10.1016/j.surfcoat.2023.130243>.
- [37] Wang SL, Chen LY, Li QL, Wang SD, Wu MY, Yang SY. Effects of Al or Mo addition on microstructure and mechanical properties of Fe-rich nonequiautomic FeCrCoMnNi high-entropy alloy. *Metals* 2022;12:191. <https://doi.org/10.3390/met12020191>.
- [38] Zin V, Montagner F, Miorin E, Mortalò C, Tinazzi R, Bolelli G, et al. Effect of Mo content on the microstructure and mechanical properties of CoCrFeNiMo<sub>x</sub> HEA coatings deposited by high power impulse magnetron sputtering. *Surf Coating Technol* 2024;476:130244. <https://doi.org/10.1016/j.surfcoat.2023.130244>.
- [39] Ai C, Zhao XB, Zhang C, Guo M, Huang TW, Zhang J, et al. Type of topologically close-packed phase in Mo-rich Ni based single crystal superalloys predicted based on ternary phase diagrams. *Chin J Nonferrous Metals* 2023;33:1074–84. <https://doi.org/10.11817/j.ysxb.1004.0609.2022-43020>.
- [40] Shun TT, Hung CH, Lee CF. The effects of secondary elemental Mo or Ti addition in Al<sub>0.3</sub>CoCrFeNi high-entropy alloy on age hardening at 700 °C. *J Alloys Compd* 2010;495:55–8. <https://doi.org/10.1016/j.jallcom.2010.02.032>.
- [41] Jang TJ, Lee YN, Ikeda YJ, Körmann F, Baek JH, Do HS, et al. Compositional role of refractory element Mo in improving strength and ductility of face-centered-cubic complex concentrated alloys. *Acta Mater* 2023;255:119030. <https://doi.org/10.1016/j.actamat.2023.119030>.
- [42] Tsau CH, Tsai MC. The effects of Mo and Nb on the microstructures and properties of CrFeCoNi (Nb, Mo) alloys. *Entropy* 2018;20:648. <https://doi.org/10.3390/e20090648>.
- [43] Jo YH, Choi WM, Sohn SS, Kim HS, Lee BJ, Lee S. Role of brittle sigma phase in cryogenic-temperature-strength improvement of non-equiautomic Fe-rich VCrMnFeCoNi high entropy alloys. *J Mater Sci Eng A* 2018;724:403–10. <https://doi.org/10.1016/j.msea.2018.03.115>.
- [44] Yan PX, Chang J, Wang WL, Zhu XN, Lin MJ, Wei B. Eutectic growth kinetics and microscopic mechanical properties of rapidly solidified CoCrFeNiMo<sub>0.8</sub> high entropy alloy. *Acta Mater* 2022;237:118149. <https://doi.org/10.1016/j.actamat.2022.118149>.
- [45] Wang WR, Wang WL, Wang SC, Tsai YC, Lai CH, Yeh JW. Effects of Al addition on the microstructure and mechanical property of Al<sub>x</sub>CoCrFeNi high-entropy alloys. *Intermetallics* 2012;26:44–51. <https://doi.org/10.1016/j.intermet.2012.03.005>.
- [46] Gao XF, Liu T, Zhang XF, Fang HZ, Qin G, Chen RR. Precipitation phase and twins strengthening behaviors of as-cast non-equiautomic CoCrFeNiMo high entropy alloys. *J Alloys Compd* 2022;918:165584. <https://doi.org/10.1016/j.jallcom.2022.165584>.
- [47] Yen CC, Lin SY, Ting CL, Tsai TL, Chen YT, Yen SK. Passivation mechanisms of CoCrFeNiMo<sub>x</sub> (x= 0, 0.1, 0.2, 0.3) high entropy alloys and MP35N in 3.5 wt% NaCl aerated aqueous solutions. *Corrosion Sci* 2024;228:111812. <https://doi.org/10.1016/j.corsci.2023.111812>.
- [48] Shun TT, Chang LY, Shiu MH. Age-hardening of the CoCrFeNiMo<sub>0.85</sub> high-entropy alloy. *J. Materials Characterization* 2013;81:92–6. <https://doi.org/10.1016/j.matchar.2013.04.012>.
- [49] Niu ZZ, Wang YZ, Geng C, Xu J, Wang Y. Microstructural evolution, mechanical and corrosion behaviors of as-annealed CoCrFeNiMo<sub>x</sub> (x= 0, 0.2, 0.5, 0.8, 1) high entropy alloys. *J Alloys Compd* 2020;820:153273. <https://doi.org/10.1016/j.jallcom.2019.153273>.